Structure, Vol. 9, 105–114, February, 2001, ©2001 Elsevier Science Ltd. All rights reserved. PII S0969-2126(01)00572-X

Computational Modeling Predicts the Structure and Dynamics of Chromatin Fiber

Daniel A. Beard and Tamar Schlick*
Department of Chemistry and
Courant Institute of Mathematical Sciences
New York University and the
Howard Hughes Medical Institute
251 Mercer Street
New York, New York 10012

Summary

Background: The compact form of the chromatin fiber is a critical regulator of fundamental processes such as transcription and replication. These reactions can occur only when the fiber is unraveled and the DNA strands contained within are exposed to interact with nuclear proteins. While progress on identifying the biochemical mechanisms that control localized folding and hence govern access to genetic information continues, the internal structure of the chromatin fiber, let alone the structural pathways for folding and unfolding, remain unknown.

Results: To offer structural insights into how this nucleoprotein complex might be organized, we present a macroscopic computer model describing the mechanics of the chromatin fiber on the polymer level. We treat the core particles as electrostatically charged disks linked via charged elastic DNA segments and surrounded by a microionic hydrodynamic solution. Each nucleosome unit is represented by several hundred charges optimized so that the effective Debye-Hückel electrostatic field matches the field predicted by the nonlinear Poisson-Boltzmann equation. On the basis of Brownian dynamics simulations, we show that oligonucleosomes condense and unfold in a salt-dependent manner analogous to the chromatin fiber

Conclusions: Our predicted chromatin model shows good agreement with experimental diffusion coefficients and small-angle X-ray scattering data. A fiber of width 30 nm, organized in a compact helical zigzag pattern with about 4 nucleosomes per 10 nm, naturally emerges from a repeating nucleosome folding motif. This fiber has a cross-sectional radius of gyration of $R_c = 8.66$ nm, in close agreement with corresponding values for rat thymus and chicken erythrocyte chromatin (8.82 and 8.5 nm, respectively).

Introduction

The internal structure of the chromatin fiber remains a mystery. Both the geometry of the linker DNA and the nucleosome packing arrangement in the fiber are unknown [1–3]. Experimental measurements, such as by electron microscopy, dynamic light scattering, and scanning force microscopy, on reconstituted small oligonucleosomes cannot determine whether the linker DNA bends or remains straight in the condensed form [2, 3]. It is speculated [4] that the linker DNA remains straight in the condensed fiber; however, the well-known solenoid model assumes that the linker DNA is bent [2, 5]. This view of straight linker DNA is supported by a recent review [3].

The atomic-level structure of a single nucleosome core particle, recently revealed at 2.8 Å resolution [6], represents a crystallographic triumph. Though offering many detailed structural features, it reveals little geometric or topological information on the packing of many nucleosomes into the 30 nm fiber. Biophysical descriptions in the spirit of polymer-level models of DNA (see, for example, [7]) can address the formidable size of a polynucleosome system and offer complementary information. Still, modeling this complex system is highly challenging: the environment of the core particle is much less regular than that of simple DNA in terms of shape and charge distribution. We address the spatial inhomogeneity by constructing an appropriate disk/bead model and the electrostatic complexity by developing a suitable discrete Debye-Hückel potential for macromolecular systems [8] that assigns several hundred charges per nucleosome so as to match the electrostatic field predicted by the nonlinear Poisson-Boltzmann equation. The combined construction is incorporated into a macro-level polymer model to offer a first-order approximation of oligonucleosome and chromatin structure.

The discrete chain model for elastic DNA was introduced by Allison [9]. Our incorporation of core particle electrostatics and the elastic mechanics of the core/linker DNA coupling requires substantial modification of the energy, force, and torque expressions. Our model also improves on earlier works on minichromosome optimization [10–12] and chromatin dynamics [13] by incorporating a finer discretization of the linker DNA (3 nm), a complete account of core particle rotations with respect to the linker DNA, and a realistic representation of the core particle electrostatics.

Our chromatin fiber is modeled as a series of N particles, with each particle representing either a linker DNA bead or a core, as depicted in Figure 1a. The core particle, including the wrapped DNA, is modeled as an idealized rigid disk, with electrostatic charges distributed on its surface. Two core particles are tethered together by 18 nm (53 bp) of linker DNA, which corresponds to about 5 full turns of the helical axis. Associated with each core particle protein–DNA complex are 277 charges (including 24 for the H3 tail) depicted as spheres of radius 0.5 nm (Figure 1a, right). The values of these charges are obtained based on the crystal structure using our algorithm described in [8]. The linker DNA is modeled by six segments of length $l_o = 3$ nm each, with electrostatic and elastic treatments following those developed for

*To whom correspondence should be addressed (e-mail: schlick@nyu.edu).

Key words: chromatin structure; nucleosome core particle; Brownian dynamics; 30 nm fiber

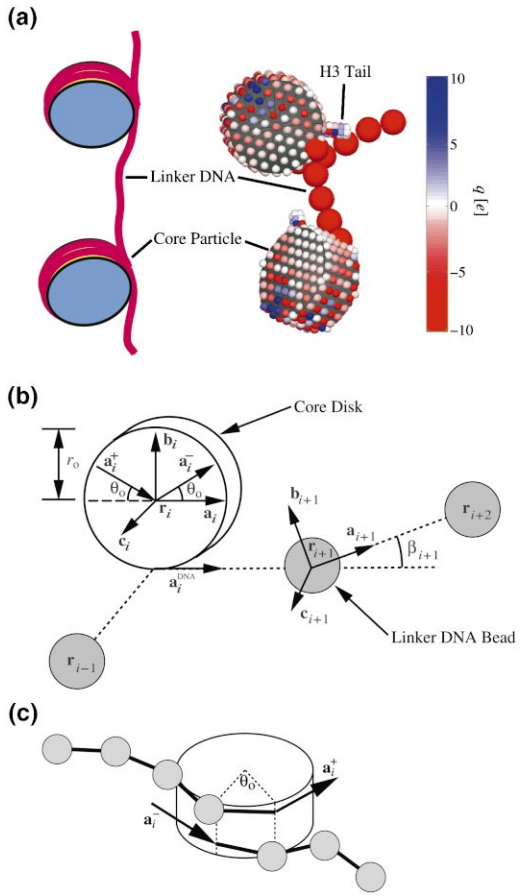

Figure 1. Chromatin Model

(a) Left: basic structure of chromatin consisting of core particles connected by linker DNA segments. Right: electrostatic parameterization of a dinucleosome model by Debye-Hückel charges placed on the core surface. The linker DNA (red beads) carries a uniform negative charge, and the core particle disks, along with the H3 tail (which extends between the gyres of the wrapped DNA [6]), are modeled by charges distributed over the surface: 253 for each nucleosome and 24 for the H3 tail. Parameterization of the charges is described in [8] .

(b) A core disk is located at position $\mathbf{r}_i$, and linker DNA beads are located at $\mathbf{r}_{i-1}$, $\mathbf{r}_{i+1}$, and $\mathbf{r}_{i+2}$. Associated with each particle is a local coordinate system denoted by the orthogonal unit vectors $\{\mathbf{a}_i, \mathbf{b}_i, \mathbf{c}_i\}$.

(c) The trajectory of the wrapped DNA exiting and entering the core disk is indicated by $\mathbf{a}_i^+$ and $\mathbf{a}_i^-$.

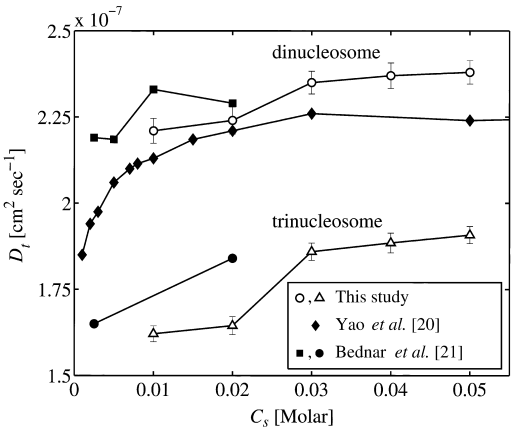

Figure 2. Calculated versus Experimental Diffusion Coefficients, D_t, Plotted as a Function of C_s, the Monovalent Salt Concentration

Computed values for dinucleosomes (open circles) and trinucleosomes (open triangles) are estimated based on 10 trajectories of length 100 ns. Error bars indicate standard error of the estimate. Also shown are data adapted from Yao et al. [20] for dinucleosomes (black diamonds) and from Bednar et al. [21] for dinucleosomes (black squares) and trinucleosomes (black circles).

superhelical DNA. We also allow the (rigid) core disk to rotate and translate in three dimensions subject to the constraint of its attachment to the linker DNA (Figure 1). The mechanics of the elastic coupling between the core particles and linker DNA segments require the fairly complex mathematical apparatus outlined in Experimental Procedures.

Linker histone H1 is not explicitly included in our present model since the physical aspects of the H1/chromatin interaction are difficult to quantify. Nor are the full lengths of the core histone tails included, as only the portions of the histone chains present in the atomic crystal model [6] are considered. Yet even with these pieces missing, this study is to our knowledge the first of its kind in which the core particle is considered at this level of detail and coupled with a realistic electrostatic treatment.

Results and Discussion

BD simulations of polynucleosome systems were performed using a numerical time step of $\Delta t = 2$ ps on an SGI Origin 2000 in serial mode. For the dinucleosome, 12 hydrodynamic particles represent 2 core particles and 2 linker chains of 5 beads (with total linker length of 18 nm). Trinucleosomes are simulated using 18 particles: 3 core particles linked in series by 18 nm chains, with each chain represented by 5 linker DNA beads. A system of 48 nucleosomes is represented by 288 particles. Each nucleosome is itself represented by 277 point charges; hence, the total number of variables in each system for electrostatic calculations is much greater than the number of hydrodynamic beads just described. The number of total beads determines the complexity of the hydrodynamic interactions, modeled by a configuration-dependent Rotne-Prager tensor; the energy function, forces, propagation protocols, and parameters are as detailed in Experimental Procedures. For calculations of 10^4 time steps (0.02 μs), the dinucleosome, trinucleosome, and 48 nucleosome systems require, respectively, 30 min, 100 min, and about 8 hr of CPU time.

Hydrodynamic Properties

The translational diffusion coefficient, D_t, of our model system was estimated from the dynamics trajectories as a function of salt by the mean square displacements of the center of mass. The center of mass is calculated from $\mathbf{r}_{cm}^n = \Sigma_{i=1}^N(\rho_i^3\mathbf{r}_i^n)/\Sigma_{i=1}^N(\rho_i^3)$, where $\mathbf{r}_i^n$ is position of bead i at time $n\Delta t$ and ρ_i is the hydrodynamic radius of bead i. D_t is calculated by $D_t = \frac{N_s\Delta t}{t_s}\sum_{j=1}^{t_s/(N_s\Delta t)}\left(||\mathbf{r}_{cm}^{(N_sj)} - \mathbf{r}_{cm}^{(N_s(j-1))}||^2/(6N_s\Delta t)\right)$, where t_s is the total simulation time

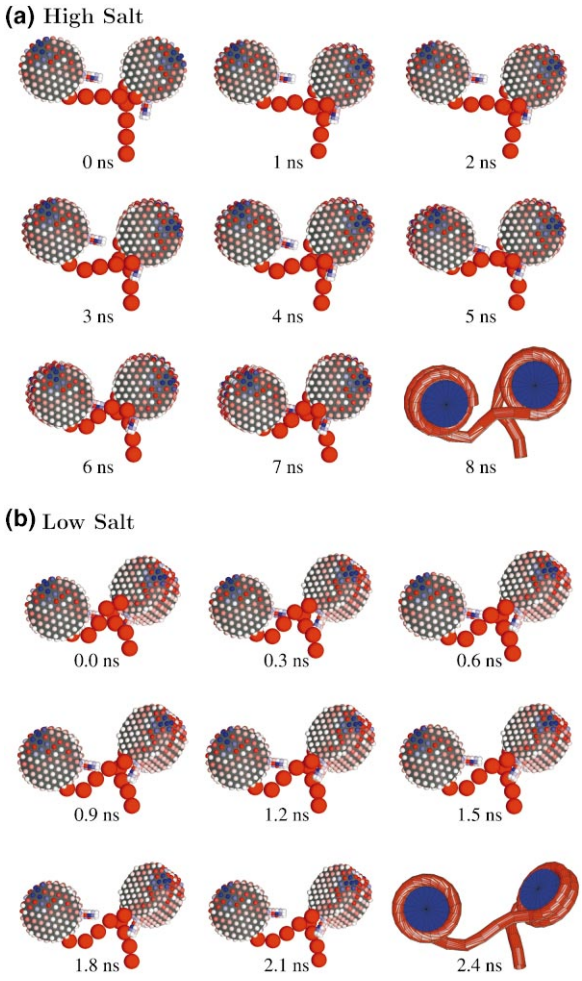

Figure 3. Dinucleosome Folding and Unfolding

(a) Simulation snapshots (1 ns intervals over an 8 ns trajectory) of a dinucleosome at the higher salt concentration of $C_s = 0.05$ M. The core particles are depicted as idealized disks with effective charges distributed on the surface. In the final frame, the linker and core DNA is depicted as a continuous chain.

(b) Snapshots of the dinucleosome at the lower salt concentration of $C_s = 0.01$ M. The initial structure is the compact for obtained at high salt.

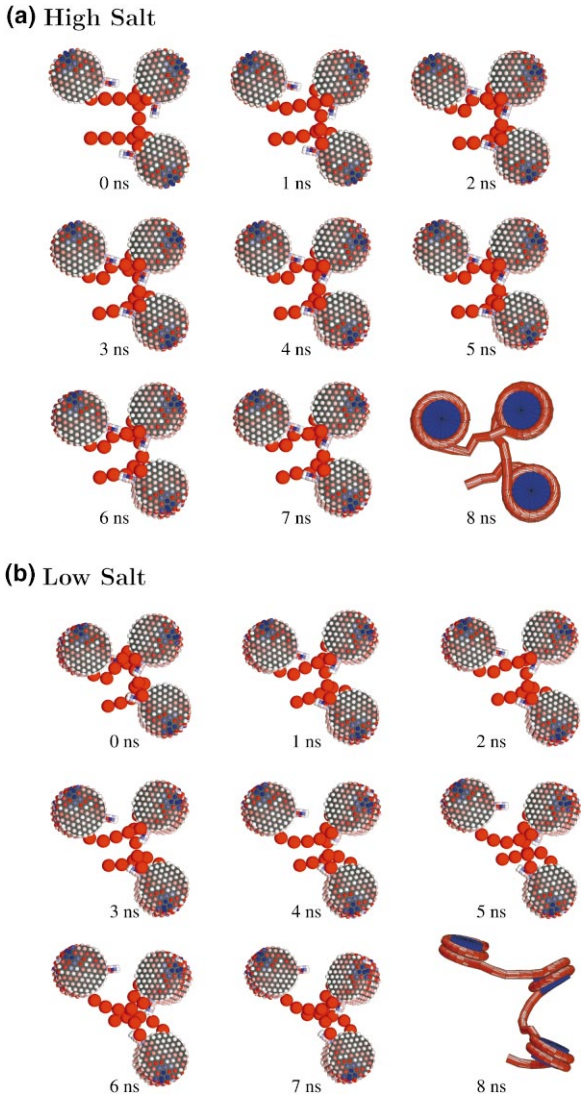

Figure 4. Trinucleosome Folding and Unfolding

(a) Simulation snapshots (1 ns intervals over an 8 ns trajectory) of a trinucleosome at the higher salt concentration of $C_s = 0.05$ M.

(b) Simulation snapshots of the trinucleosome at the lower salt concentration of $C_s = 0.01$ M. The initial structure is the compact form of the trinucleosome obtained at $C_s = 0.05$ M. The final structure is rotated 90° relative to the other snapshots.

and N_s is the number of time steps between calculations of mean square displacement. A simulation extending to $t_s = 0.1$ μs was used, and N_s was set to 100 steps. A total of 10 independent trajectories was used for each estimate. For supercoiled DNA, both experimental and simulation work has demonstrated the compaction of long, topologically constrained DNA at high salt [14–18]. For chromatin, the details of such salt effects remain unresolved. Namely, measured diffusion and sedimentation coefficients for dinucleosome particles reveal a small [19, 20] or negligible [21, 22] increase in these constants over the limited range of $C_s = 0.001$–0.020 M NaCl, but a more pronounced increase for 3–5 oligonucleosome units. Thus, cooperative effects of nucleosome assembly may lead to changes in tertiary organization.

The estimated diffusion coefficients are plotted as function of C_s in Figure 2 for dinucleosomes and trinucleosomes. Also shown are data adapted from Yao et al. [20] and Bednar et al. [21]. For each system, the computed D_t increases with the salt concentration. For dinucleosomes, the experimental measurements of D_t range from about 1.9×10^{-7} to 2.3×10^{-7} cm^2 s^{-1} [19–21]. Data measured for chicken erythrocyte dinucleosomes [19] show that D_t increases approximately 16% over an 18-fold range in monovalent salt concentration: 1.95×10^{-7} cm^2 s^{-1} at $C_s = 0.001$ M to about 2.25×10^{-7} cm^2 s^{-1} at $C_s = 0.018$ M.

Other measurements [21] show no significant increase over a similar range of salt concentration on dinucleosomes but an increase in D_t for trinucleosome and larger systems with increasing salt concentration. Conclusions

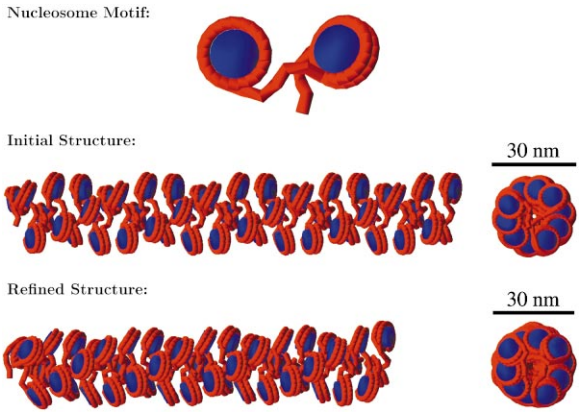

Figure 5. Model for the 30 nm Fiber

Upper panel shows the nucleosome folding motif obtained for condensed dinucleosome at C_s = 0.05 M. The 48 nucleosome system in the middle panel is constructed from the repeating nucleosome motif above. A 50 ns Brownian dynamics trajectory at C_s = 0.05 M, applied to the initial structure, produces the refined structure illustrated in the lower panel. The images to the right are side views demonstrating the diameter of the fiber.

drawn from these measurements, as well as from cryo-electron microscopy data and other hydrodynamics studies [22], are that the linker remains straight. This implies that the dinucleosome is not likely to condense at high salt concentration and that the salt-dependent increase in trinucleosome mobility is likely due to a collapse in the angle formed by the three core particles [3, 21].

Our estimates of D_t show an increase with salt concentration for dinucleosomes less drastic than that measured by the first group [19, 20]. The estimates for trinucleosomes show a sharp increase in D_t from C_s = 0.02 to C_s = 0.3 M, similar in magnitude to the observations of the second group [21]. The structural basis for these observations emerges from our folding simulations of dinucleosome and trinucleosome dynamics.

Dinucleosome and Trinucleosome Dynamics

Figure 3 shows snapshots from an 8 ns BD trajectory for a dinucleosome system at high (C_s = 0.05 M) and low (C_s = 0.01 M) salt concentrations. At high salt, the dinucleosome spontaneously folds in just a few nanoseconds into a stable condensed structure in which linker DNA bending is facilitated by association with the positively charged H3 tail. The core particles do not make close contact as required by most solenoidal models for the 30 nm fiber [5, 23, 24], yet the center-to-center distance between the core particles decreases from 18 nm (initial structure) to about 16 nm in the condensed structure.

Starting from this folded structure at low salt of C_s = 0.01 M (Figure 3B), the linker DNA straightens and the dinucleosome adopts an extended form. These salt-

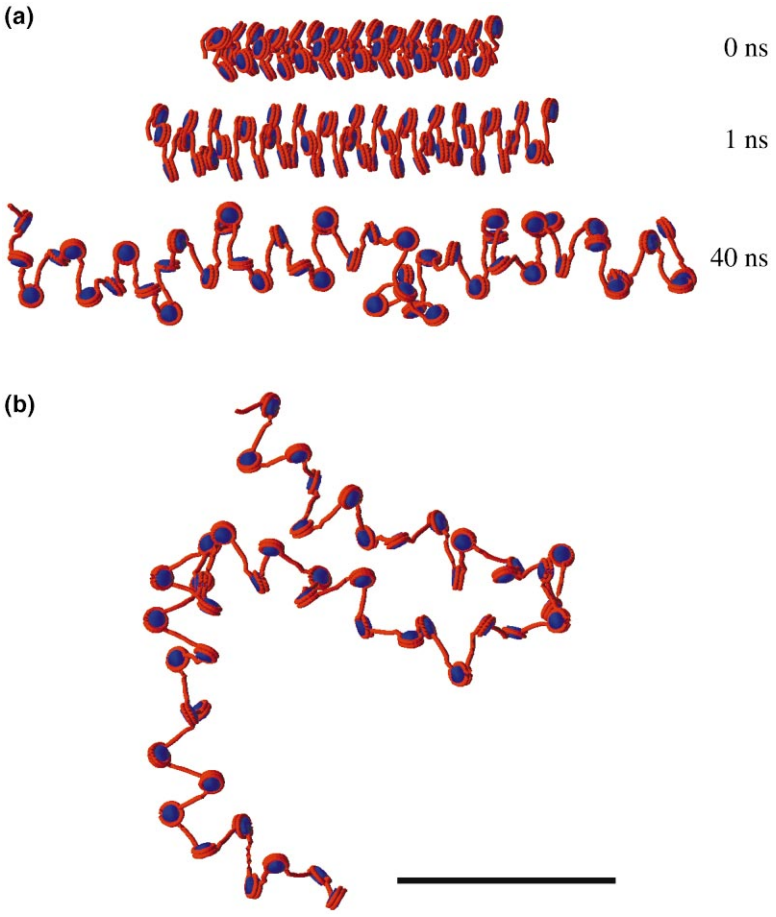

Figure 6. Instability of the 30 nm Fiber at Low Salt Demonstrated by BD Simulation

(a) Using the refined condensed structure obtained at C_s = 0.05 M as the initial condition (Figure 5), the 48 nucleosome fiber unfolds at C_s = 0.01 M.

(b) The low-salt equilibrium structure for the 48 nucleosome fiber obtained by Monte Carlo sampling. A comparison to the high salt condensed fiber (top) reveals a difference of several orders of magnitude. The scale bar is 100 nm.

dependent structures account for the values of D_t reported in Figure 2.

The folding snapshots for a trinucleosome at C_s = 0.05 M in Figure 4a show again how the linker DNA bends to optimize contacts with the H3 tail. In the final structure, both the bending of linker DNA and the center-to-center distance of consecutive core particles are similar to those observed for the dinucleosome at high salt. Thus, the mechanism of condensation is analogous, although the salt-dependent increase in D_t is more apparent for trinucleosomes than dinucleosomes. The core particles do not contact one another, and the final structure shown in Figure 4a remains relatively stable. At low salt (Figure 4B), this compact trinucleosome unfolds quickly, with the linkers straightening and the distance between core particles increasing.

A Model for the 30 nm Fiber

From the condensed structural motif of the dinucleosome (Figure 5, top), we construct a model for the condensed structure of larger polynucleosome systems. Namely, the position of the second core particle ($\mathbf{r}_6$) is determined relative to the location and orientation of the first core particle ($\mathbf{r}_1$) according to $\mathbf{r}_6 = \mathbf{r}_1 + (16.2\text{ nm})\mathbf{a}_1 + (3.7\text{ nm})\mathbf{b}_1 - (0.8\text{ nm})\mathbf{c}_1$, with the rotation transforming $\{\mathbf{a}_1, \mathbf{b}_1, \mathbf{c}_1\}$ to $\{\mathbf{a}_6, \mathbf{b}_6, \mathbf{c}_6\}$ defined by the Euler angles $\alpha = -3.13$, $\beta = 1.87$, and $\gamma = 3.73$ radians. The angle formed between the flat surfaces of the core disks is calculated from $\arccos(\mathbf{c}_1 \cdot \mathbf{c}_6)$, which is about 33°. A 48 nucleosome structure obtained based on the repeating motif is shown in the upper panel of Figure 5. This structure is a regular helix with a period of about 3.1 nucleosomes per turn. The refined structure obtained from a 50 ns BD trajectory based on this initial model increases the compaction of the fiber as a given core particle is brought into close proximity to its third neighbor in both directions along the chain. The core/core binding interactions, due to favorable electrostatic interactions between the core surfaces, form a chain that wraps around the fiber in a left-handed helix.

The refined structure of Figure 5 has a packing ratio of about 4 nucleosomes per 10 nm and a cross-sectional radius of gyration of R_c = 8.66 nm. The predicted value of R_c is strikingly close to experimental measures for rat thymus chromatin, R_c = 8.82 nm [25, 26], and chicken erythrocyte chromatin, $R_c \cong$ 8.5 nm [27].

Unfolding at Low Salt

As a further test of our predicted fiber structure, we examine its behavior at low salt concentration. The fiber unravels at C_s = 0.01 M (Figure 6A), and the higher order organization of the fiber disappears. In the early part of the simulation, the unscreened DNA charges repel one another and the fiber quickly expands, like an accordion. Once the initial instability is relieved, motions are slower and are driven mainly by entropy.

The low-salt equilibrium structure shown in Figure 6b was obtained from Metropolis Monte Carlo sampling [28] of the structure at C_s = 0.01 M. The equilibrium structure resembles the disordered zigzag observed at low salt by Bednar et al. [29]. (Compare Figure 6b to Figure 1 of [29].)

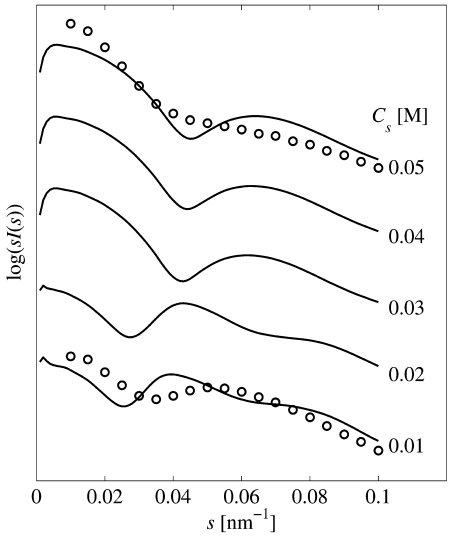

Figure 7. Calculated Small-Angle X-Ray Scattering Profiles for 48 Nucleosome Systems at Salt Concentrations Ranging from 0.01 M to 0.05 M

The scattered X-ray intensity was calculated as a function of s according to the Debye formula [50]: $I(s) = \Sigma_{i,j}\, f_i(s) f_j(s) \sin 2\pi s r_{ij} / (2\pi s r_{ij})$, where $s = (2\sin\theta)/\lambda$, θ is the scattering angle, and λ is the X-ray wavelength. For our purpose, each particle in the system was treated as a symmetric Gaussian subunit, with structure factor $f_i(s) = R_i^3 \exp[-(\pi s R_i)^2]$. The effective radius R_i is set to R_i = 1.5 nm for linker beads and R_i = 4.5 nm for core particles. Scattering profiles were calculated as the mean intensity based on 100 independent equilibrium configurations for each salt concentration. Computed data plotted as log $s(I(s))$ versus s are shown as solid lines. The profiles obtained by Fujiwara [26] at 0.01 and 0.05 M salt concentration are shown as circles. The profiles are displaced vertically for clarity.

Small Angle X-Ray Scattering

These structural predictions of the chromatin fiber at high and low salt can also be compared to small-angle X-ray scattering profiles for the 48 nucleosome chromatin systems as done for supercoiled DNA [16] (see caption to Figure 7) The computed profiles are plotted in Figure 7 along with data from [26] (open circles) for rat thymus chromatin as $\log(I(s))$ versus $s = (2\sin\theta)/\lambda$, where θ is the scattering angle, λ is the X-ray wavelength, and I is the intensity. The curves plotted in Figure 7 reflect averages of the scattering profiles obtained from an ensemble of 100 equilibrium structures at each salt concentration. Each ensemble was obtained via Monte Carlo [28] sampling of the configurational space.

At low salt, a peak centered at 25 nm (0.04 nm^{-1}) is observed. This peak corresponds to the mean core center-to-center distance for the extended structure. As observed experimentally [25, 26], the peak shifts to higher values of s as salt concentration increases and the structure condenses. Our computed profiles at C_s = 0.03, 0.04, and 0.05 M are nearly identical, reflecting of the stability of the condensed structure at these salt environments. The peak observed at 0.06 nm^{-1} for C_s = 0.05 M is not apparent in the experimentally obtained profile, indicating that our predicted structure may be more ordered than the actual 30 nm fiber.

Table 1. Elastic and Geometric Parameters Used in the Dinucleosome Model

Parameter	Description	Value
l_o	Equilibrium segment length	3.0 nm
h	Stretching constant	5000 k_BT/l_o^2
C	Twisting rigidity constant	3.0×10^{-12} erg·nm
L_p	Elastic bending persistence length of DNA	50 nm
θ_o	Angular separation between linker segments	90°
r_o	Radius of wound DNA supercoil	4.8 nm
$2\omega_o$	Width of wound DNA supercoil	3.6 nm
ρ_i, $i \in I_l$	Hydrodynamic radius of linker bead (set I_l)	1.5 nm
ρ_i, $i \in I_c$	Hydrodynamic radius of core bead (set I_c)	5 nm
k_{ex}	Excluded volume parameter	0.001
σ_1	Core/linker excluded volume parameter	3.0 nm
σ_2	Core/core excluded volume parameter	2.0 nm
Δt	Numerical time step for dynamics simulation	2.0 ps

Summary

Our macroscopic model for approximating the internal structure and dynamics of the chromatin fiber, based on the well characterized discrete segment model for superhelical DNA, discrete parameterization of the electrostatics associated with the core particle, and sophisticated mathematical machinery to describe the mechanics of polynucleosomes subject to systematic and hydrodynamic forces, conforms to a diverse set of experimental observations:

1. The predicted translation diffusion coefficients for dinucleosomes and trinucleosomes increase with salt concentration, with the increase for trinucleosome more pronounced than for dinucleosomes [19–21].
2. At low monovalent concentrations ($C_s \leq 0.02$ M), the linker segments remain relatively straight [1–3] due to low electrostatic shielding. Our model adopts a disordered global zigzag conformation, similar to experimental observations [29].
3. At higher salt concentration ($C_s = 0.05$ M), the linker DNA bends and core particles are brought into closer proximity [19, 20]. Condensation for small systems (two and three nucleosomes) occurs rapidly.
4. The repeating condensed nucleosome motif, observed for small polynucleosome systems, results in a 30 nm diameter fiber for larger systems at $C_s \geq 0.03$ M, as observed experimentally. The cross-sectional radius of gyration of the fiber $R_c = 8.66$ nm agrees well with experimental measurements for chicken erythrocyte and rat thymus chromatin [25–27].
5. The predicted condensed 30 nm fiber structure is unstable at low salt concentration and consequently unfolds.
6. Electrostatic charges on the core protein are responsible for modulating fiber condensation; see [30] and references therein.
7. Simulated small-angle X-ray scattering profiles show a characteristic peak for our chromatin fiber at 25 nm (0.04 nm^{-1}) for low salt conformations. This peak shifts to higher angles as the salt concentration increases and the structure condenses [25, 26].

Table 2. Electrostatic Parameters for DNA

C_s [Molar]	ν [e/nm]	κ [1/nm]
0.01	−2.43	0.330
0.02	−2.96	0.467
0.03	−3.39	0.572
0.04	−3.91	0.660
0.05	−4.15	0.738

Our predicted 30 nm fiber structure (Figure 5) agrees with recently proposed models in which the linker DNA remains extended [3, 4, 29] and is similar to the crossed-linker class of models [31–33] in which the linker DNA passes through the center of the fiber. Additionally, the predicted fiber bears some similarity to the classic solenoid model [5] in that core particles are wound around the axis of the fiber as a regular helix. Thus, the straight-linker/zigzag motif does not preclude a regular periodic organization of nucleosomes in the 30 nm fiber. The linker DNA bends, but more gently than in the standard solenoid models [2].

The repeating nucleosome motif is similar to the nucleosome/linker DNA/linker histone structural motif proposed by Bednar et al. [29] as a basis for higher order folding of the fiber. They suggested, based on cryoelectron microscopy observations, that the two linker DNA segments attached to a core particle remain in close contact for a few nanometers beyond the core, likely due to binding with H1 linker histone. Experiments suggest that H1 helps maintain the exiting and entering linker DNA in close proximity [1, 3, 29]. This effect could be incorporated into the potential energy function with additional attractive forces between the exiting and entering linker segments.

Applications are underway to elucidate the mechanisms by which the modulation of the electrostatic charge density on the surface of the core particle governs chromatin structure and thus plays a key role in the initiation of transcription. For example, removal of the positively charged basic tails from the core particle undermines the stability of the condensed structure in the absence of the linker histone H1 [34]. In addition, transcriptionally silent domains in yeast contain hypoacetylated core histone H4 [35], while histone acetylation has been shown to be associated with transcription in a wide range of species and cell types [36–40]. Modeling these biochemical modifications of the core proteins requires a reparameterization of the core particle effective charges following the same protocol of optimizing the effective surface charges, as we describe in [8]. In

addition, the methodology outlined here and in [8] can be used to construct models for other protein–DNA complexes, such as resolvase-DNA system [41].

Biological Implications

We have constructed a polymer-level computational model for the chromatin fiber in which the electrostatic and structural properties of the core particle and linker DNA are incorporated into polynucleosome systems of various sizes. Our model thus efficiently integrates atomic-level details of a biomolecule into an accurate biophysical description of a system too large to treat on the atomic scale. Computed small-angle X-ray scattering profiles and hydrodynamic properties serve as criteria for judging the validity of our predicted structures. Simulations reveal salt-dependent condensation analogous to the chromatin fiber. Our predicted compact helical zigzag for the internal structure of the compact fiber, a form which represses transcription and replication, has dimensions and features in excellent agreement with experiment. The forces that modulate fiber condensation are electrostatic and thus can be biochemically regulated via phosphorylation, acetylation, and other posttranscriptional modifications that are known to be associated with various genetic pathways. Thus, further studies with our model can offer systematic structural and dynamic data to compliment experimental observations on fundamental biological processes associated with genomic packaging and transcription.

Experimental Procedures

Mathematical Model for the Structure and Dynamics of Chromatin

This section outlines the mathematical representation of the chromatin fiber model (configurational variables and potential energy function) and the Brownian Dynamics (BD) propagation scheme. A complete description of the methodology, including analytic expressions for the forces and torques associated with the potential energy function and simulation algorithm, is available at http://monod.biomath.nyu.edu/index/chromatin_supplement/index.html.

Model Geometry

The model structure is illustrated in Figure 1. Each core particle disk is connected to one or two linker DNA segments (see Figure 1b). In Figure 1b, $\mathbf{r}_i$ denotes the position of the center of a core disk, while $\mathbf{r}_{i-1}$, $\mathbf{r}_{i+1}$, and $\mathbf{r}_{i+2}$ denote positions of linker DNA beads. The orientation of the core disk is specified by a local coordinate system $\{\mathbf{a}_i, \mathbf{b}_i, \mathbf{c}_i\}$ where the unit vectors $\mathbf{a}_i$ and $\mathbf{b}_i$ lie in the plane of the flat surface of the disk, and $\mathbf{c}_i = \mathbf{a}_i \times \mathbf{b}_i$. The attachment of the linker DNA to the core particle is illustrated in Figure 1. The linker DNA enters the core particle at the position $\mathbf{r}_i - r_o[\mathbf{b}_i \cos\theta_o - \mathbf{a}_i \sin\theta_o] + w_o\mathbf{c}_i$ and exits at position $\mathbf{r}_i - r_o\mathbf{b}_i - w_o\mathbf{c}_i$. The scalar parameters r_o, w_o, and θ_o are determined by the geometry of the wrapped DNA supercoil. Based on the crystal structure [6], we set the values of these parameters as follows: $r_o = 4.8$ nm, $w_o = 1.8$ nm, and $\theta_o = 90^\circ$ (see Table 1).

A local coordinate system $\{\mathbf{a}_j, \mathbf{b}_j, \mathbf{c}_j\}$ is also associated with each linker bead position, $\mathbf{r}_j$, and is used to calculate the local torsion on the linker beads. We define the sets I_c and I_l to be, respectively, the set of core beads and the set of linker DNA beads. The vectors $\{\mathbf{a}_i\}$ for $i \in I_l$ are directed in the direction of the linker DNA segment:

$$\mathbf{a}_i = \begin{cases} (\mathbf{r}_{i+1} - \mathbf{r}_i)/||\mathbf{r}_{i+1} - \mathbf{r}_i|| & \text{for } i+1 \in I_l \\ \dfrac{\mathbf{r}_{i+1} - r_o(\mathbf{b}_{i+1}\cos\theta_o - \mathbf{a}_{i+1}\sin\theta_o) + w_o\mathbf{c}_{i+1} - \mathbf{r}_i}{||\mathbf{r}_{i+1} - r_o(\mathbf{b}_{i+1}\cos\theta_o - \mathbf{a}_{i+1}\sin\theta_o) + w_o\mathbf{c}_{i+1} - \mathbf{r}_i||} & \text{for } i+1 \in I_c \end{cases} \quad (1)$$

Since the wrapped DNA does not make two full turns around the core disk, the unstressed trajectory of $\mathbf{a}_{i-1}$ is not parallel to $\mathbf{a}_i$ when the i^{th} bead is a disk. The trajectory of the wrapped DNA is denoted $\mathbf{a}_i^-$ (see Figure 1c) and is calculated as $\mathbf{a}_i^- = \mathbf{a}_i\cos\theta_o + \mathbf{b}_i\sin\theta_o$. Similarly, the trajectory of the wrapped DNA, as it exits the core is denoted by $\mathbf{a}_i^+$. The local coordinate systems of the wrapped DNA entering and exiting the core particle are given by:

$$\begin{aligned} \mathbf{a}_i^- &= \mathbf{a}_i\cos\theta_o + \mathbf{b}_i\sin\theta_o \\ \mathbf{b}_i^- &= -\mathbf{a}_i\sin\theta_o + \mathbf{b}_i\cos\theta_o \\ \mathbf{c}_i^- &= \mathbf{c}_i \end{aligned} \quad (2)$$

and $\{\mathbf{a}_i^+, \mathbf{b}_i^+, \mathbf{c}_i^+\} = \{\mathbf{a}_i, \mathbf{b}_i, \mathbf{c}_i\}$. For the core particle, we introduce the vectors $\{\mathbf{a}_i^{DNA}, \mathbf{b}_i^{DNA}, \mathbf{c}_i^{DNA}\}$ (see Figure 1), to represent the local coordinate system associated with the DNA segment connecting the core at $\mathbf{r}_i$ and the linker vertex $\mathbf{r}_{i+1}$. The calculation of $\{\mathbf{a}_i^{DNA}, \mathbf{b}_i^{DNA}, \mathbf{c}_i^{DNA}\}$ is outlined next.

Euler Angles

The bending and twisting terms in the potential energy function are expressed in terms of the Euler angles [42], $\{\alpha_i, \beta_i, \gamma_i\}$, that transform one local coordinate system to the next. In the following sections, we will make use of the following sets of Euler angles:

- For i, $i+1 \in I_l$, the angles $\{\alpha_i, \beta_i, \gamma_i\}$ transform from the $\{\mathbf{a}_i, \mathbf{b}_i, \mathbf{c}_i\}$ to the $\{\mathbf{a}_{i+1}, \mathbf{b}_{i+1}, \mathbf{c}_{i+1}\}$ coordinate system.
- For $i+1 \in I_c$, the angles $\{\alpha_i, \beta_i, \gamma_i\}$ transform from the $\{\mathbf{a}_i, \mathbf{b}_i, \mathbf{c}_i\}$ to the $\{\mathbf{a}_{i+1}^-, \mathbf{b}_{i+1}^-, \mathbf{c}_{i+1}^-\}$ coordinate system.
- For $i \in I_c$, the angles $\{\alpha_i^+, \beta_i^+, \gamma_i^+\}$ transform $\{\mathbf{a}_i^+, \mathbf{b}_i^+, \mathbf{c}_i^+\}$ to $\{\mathbf{a}_i^{DNA}, \mathbf{b}_i^{DNA}, \mathbf{c}_i^{DNA}\}$, and the angles $\{\alpha_i, \beta_i, \gamma_i\}$ transform $\{\mathbf{a}_i^{DNA}, \mathbf{b}_i^{DNA}, \mathbf{c}_i^{DNA}\}$ to $\{\mathbf{a}_{i+1}, \mathbf{b}_{i+1}, \mathbf{c}_{i+1}\}$.

The additional DNA coordinate system associated with each core bead, $\{\mathbf{a}_i^{DNA}, \mathbf{b}_i^{DNA}, \mathbf{c}_i^{DNA}\}$, and the associated Euler angles $\{\alpha_i^+, \beta_i^+, \gamma_i^+\}$, are calculated based on the assumption that the core particle protein–DNA complex remains rigid, and twisting of the DNA that is wrapped around the core does not contribute to the mechanics of the model. Therefore, $\alpha_i^+ = -\gamma_i^+$ Calculations of the vector $\mathbf{a}_i^{DNA}$ and the angle β_i^+ are straightforward:

$$\mathbf{a}_i^{DNA} = \frac{\boldsymbol{r}_{i+1} - \boldsymbol{r}_i + r_o\boldsymbol{b}_i + w_o\boldsymbol{c}_i}{||\boldsymbol{r}_{i+1} - \boldsymbol{r}_i + r_o\boldsymbol{b}_i + w_o\boldsymbol{c}_i||}, \quad (3)$$

$$\beta_i^+ = \cos^{-1}(\mathbf{a}_i^+ \cdot \mathbf{a}_i^{DNA}). \quad (4)$$

We calculate α_i^+ from:

$$\alpha_i^+ = \begin{cases} |\alpha_i| \text{ for } \mathbf{c}_i^+ \cdot \left((\mathbf{a}_i^{DNA} - \cos\beta_i^+\mathbf{a}_i^+)/\sin\beta_i^+\right) > 0 \\ -|\alpha_i| \text{ for } \mathbf{c}_i^+ \cdot \left((\mathbf{a}_i^{DNA} - \cos\beta_i^+\mathbf{a}_i^+)/\sin\beta_i^+\right) < 0, \end{cases} \quad (5)$$

where

$$|\alpha_i^+| = \cos^{-1}\left[\mathbf{b}_i^+ \cdot \left(\frac{\mathbf{a}_i^{DNA} - \cos\beta_i^+\mathbf{a}_i^+}{\sin\beta_i^+}\right)\right]. \quad (6)$$

We set $\gamma_i^+ = -\alpha_i^+$ to ensure that no torsion is introduced into the Euler rotation $\{\alpha_i^+, \beta_i^+, \gamma_i\}$. Then the Euler rotations are applied to $\{\mathbf{a}_i^+, \mathbf{b}_i^+, \mathbf{c}_i^+\}$ to obtain $\mathbf{b}_i^{DNA}$ and $\mathbf{c}_i^{DNA}$.

Calculation of the Potential

The energy associated with a given polymer structure is estimated from the sum of several elastic energy terms, an electrostatic potential, and an excluded volume term [43]:

$$E = E_S + E_T + E_B + E_C + E_V. \quad (7)$$

The first three terms represent elastic contributions from stretching, twisting, and bending, respectively. The terms E_C and E_V are used to model electrostatic and excluded volume interactions, respectively.

Stretching

The stretching potential, E_S, is a computational device, and its treatment is optimized with respect to the time step of the dynamics simulation [44], so as to balance realized deviations from the target length with the computational time step. E_S is written as:

$$E_S = \frac{h}{2}\sum_{i=1}^{N-1}(l_i - l_o)^2 \quad (8)$$

where l_i is the length of the segment connecting particle i to particle $i+1$, calculated as:

$$l_i = \begin{cases} ||\mathbf{r}_{i+1} - \mathbf{r}_i + r_o\mathbf{b}_i + w_o\mathbf{c}_i|| & \text{for } i \in I_c \\ ||\mathbf{r}_{i+1} - r_o\mathbf{b}_{i+1}^- + w_o\mathbf{c}_{i+1}^- - \mathbf{r}_i|| & \text{for } i+1 \in I_c \\ ||\mathbf{r}_{i+1} - \mathbf{r}_i|| & \text{otherwise.} \end{cases} \quad (9)$$

We use an equilibrium segment length of $l_o = 3$ nm, which corresponds to roughly 9 bp per segment.

It has been shown for the BD simulation of linear and circular DNA [44] that a choice of $h = 100k_BT / l_o^2$, where k_B is Boltzmann's constant and T is the absolute temperature, results in standard deviations in segment length of around 10% of l_o. The motions of the relatively large nucleosome beads in the present model tend to produce greater stretching and compressive forces on the linker DNA than are typically found in supercoiled DNA alone. This means that a greater value for the stretching rigidity constant is required to achieve comparable accuracy. A value of $h = 5000k_BT / l_0^2$ results in segment length deviations of less than 2% of the equilibrium segment length and a mean segment length equal to the equilibrium segment length for time steps of 2 ps.

Twisting

The torsional rotation about the segment connecting particles i and $(i+1)$ is given by the sum of the Euler angles $\alpha_i + \gamma_i$, and the torsional energy, E_T, is calculated from:

$$E_T = \frac{C}{2l_o}\sum_{i=1}^{N-1}(\alpha_i + \gamma_i)^2, \quad (10)$$

where C is the torsional rigidity constant.

Bending

The bending energy, E_B, is calculated from the set of angles denoting the deformation between the linker DNA segments.

$$E_B = \frac{g}{2}\sum_{i=1}^{N-1}(\beta_i)^2 + \frac{g}{2}\sum_{i\in I_c}(\beta_i^+)^2, \quad (11)$$

The bending constant, g, can be calculated from:

$$g = L_p k_B T / l_o, \quad (12)$$

where L_p is the bending persistence length.

Electrostatics

Representative charges are assigned to the linker beads as well as on the surface of the core disks. The assignment of charges in the model is based on a discrete N-body potential that approximates the solution to the nonlinear Poisson-Boltzmann equation in the solvent surrounding the core particle. This procedure is detailed in Beard and Schlick [8]. A single charge, q_l, is assigned to each linker bead, and a set of charges $\{q_c^k\}$ is assigned to each core disk, where the index k refers to the k^{th} charge on the core disk. The position of the k^{th} charge on the j^{th} particle is denoted by $\{\mathbf{x}_c^{jk}\}$ for $j \in I_c$.

The charge on a linker bead is calculated as $q_l = \nu l_o$, where ν is the effective linear charge density on DNA, calculated by fitting the tail of the Debye-Hückel potential for an infinitely long cylinder to the Gouy-Chapman potential in the far zone [45]. Values for ν and κ, the inverse Debye length for various levels of monovalent salt concentration, are listed in Table 2.

The electrostatic contribution to the potential is calculated as the superposition of the fundamental solution to the linearized Poisson-Boltzmann equation:

$$E_C = \sum_{\substack{j>i+1 \\ i,j\in I_l}} \frac{q_l^2 e^{-\kappa r_{ij}}}{\epsilon r_{ij}} + \sum_{\substack{j>i+1 \\ i\in I_l, j\in I_c}} \left[\sum_{k=1}^{N_c} \frac{q_l q_c^k e^{-\kappa r_{i\{jk\}}}}{\epsilon r_{i\{jk\}}}\right] + \sum_{\substack{j>i+1 \\ i,j\in I_c}} \left[\sum_{k=1}^{N_c}\sum_{l=1}^{N_c} \frac{q_c^k q_c^l e^{-\kappa r_{\{ik\}\{jl\}}}}{\epsilon r_{\{ik\}\{jl\}}}\right], \quad (13)$$

where κ denotes the inverse Debye length (salt dependent), ϵ is the dielectric constant of the medium, and N_c is the number of point charges on each core disk. In equation (13), we have introduced the notation $r^{ij} = \|\mathbf{r}_j - \mathbf{r}_i\|$ to denote the distance between the centers of the i^{th} and j^{th} particles. Similarly, the distance between the center of the i^{th} particle and the k^{th} charge on particle $j \in I_c$ is denoted by $r_{i\{jk\}} = ||\mathbf{x}_c^{jk} - \mathbf{r}_i||$; and the distance between the k^{th} charge on particle $i \in I_c$ and the l^{th} charge on particle $j \in I_c$ is denoted by $r_{\{ik\}\{jl\}} = ||\mathbf{x}_c^{ik} - \mathbf{x}_c^{jl}||$.

The first term in equation (13) is due to linker/linker interactions, and the summation is over all pairs of linker beads. The summation in the second term is over all linker/core pairs and in the last term over all core/core pairs.

Excluded Volume

It is necessary to include an excluded volume term in the calculation of the potential to avoid the overlap of positive and negative charges. We represent the excluded volume potential, E_V, as the sum of Lennard-Jones potentials arising from linker/core pair interactions and from core/core pair interactions as

$$E_V = k_{ex}k_BT \sum_{\substack{j>i \\ i\in I_l, j\in I_c}} \left[\sum_{k=1}^{N_c}\left(\frac{\sigma_1}{r_{i\{jk\}}}\right)^{12} - \left(\frac{\sigma_1}{r_{i\{jk\}}}\right)^{6}\right] + k_{ex}k_BT \sum_{\substack{j>i \\ i,j\in I_c}} \left[\sum_{k=1}^{N_c}\sum_{l=1}^{N_c}\left(\frac{\sigma_2}{r_{\{ik\}\{jl\}}}\right)^{12} - \left(\frac{\sigma_2}{r_{\{ik\}\{jl\}}}\right)^{6}\right]. \quad (14)$$

The terms in equation (14) have a shallow minimum of value $-k_{ex}k_BT / 4$ at a separation between charges of $2^{1/6}\sigma$, where σ and k_{ex} are the parameters describing the Lennard-Jones interactions.

The excluded volume parameters (see Table 1) are chosen to ensure that particles do not overlap one another over the course of a simulation. It is not necessary to include a linker/linker excluded volume term because the electrostatic repulsion between DNA segments proves sufficient to prevent overlap.

Brownian Dynamics Algorithm

The BD algorithm [46] for rotational and translational motions can be expressed as

$$\Delta\Omega_i^n = \frac{\Delta t}{\xi_i}(\tau_i + \omega_i)$$
$$\mathbf{r}^{n+1} = \mathbf{r}^n + \frac{\Delta t}{k_BT}\mathbf{D}(\mathbf{r}^n)\cdot\mathbf{f}^n + \mathbf{w}^n, \quad (15)$$

where Δt is a finite time step, k_B is Boltzmann's constant, and T is the absolute temperature. In equation (15), $\Delta\Omega_i^n$ is a finite rotation about the i^{th} rotational degree of freedom at the n^{th} time step, and $\mathbf{r}^n \in \Re^{3N}$ is the collective position vector for the N particles in the system. Hydrodynamic interactions with the solvent are specified by the rotational friction coefficients $\{\xi_i\}$ and the configuration-dependent diffusion tensor $\mathbf{D}(\mathbf{r}^n)$. Associated with the intramolecular potential energy function are the systematic forces $\mathbf{f}^n$ and torques τ^n acting at the n^{th} time step. Equation (15) also includes the stochastic terms ω_i^n and $\mathbf{w}^n$, which are white noise processes used to model thermal interactions with the solvent. The correlation structure of the white noise terms is related to the hydrodynamic interactions by

$$\langle \tau_i^n \tau_i^m \rangle = 2k_BT\xi_i\delta_{nm}$$
$$\langle (\mathbf{w}^n)(\mathbf{w}^m)^T \rangle = 2\Delta t\mathbf{D}(\mathbf{r}^n)\delta_{nm}, \quad (16)$$

where δ_{nm} is the Kronecker delta function.

For detailed methodology, see the supplementary material (http://monod.biomath.nyu.edu/index/chromatin_supplement/index.html).

Setup and Model Parameters

We chose reasonable parameter values from the literature wherever possible. Table 1 lists the elastic and geometric parameters used in the model. The electrostatic parameters discussed above are derived based on a detailed analysis of the solvated core particle [8]. A reasonably accepted value for the twisting energy constant

is $C = 3.0 \times 10^{-12}$ erg nm [47], which corresponds to a twisting persistence length of about 75 nm. The bending rigidity constant is calculated from equation (12) based on the persistence length of DNA, set here to be 50 nm, which yields $g = 6.9 \times 10^{-13}$ erg. This value is consistent with recent measures of the nonelectrostatic contribution to the bending rigidity (i.e., the high salt limit of the persistence length) [48].

We note that there exists a wealth of physiochemical data suggesting a substantially lower value for the nonelectrostatic contribution to the effective bending rigidity of DNA. See, for example, Eisenberg [49], which reviews measurements of DNA flexibility based on hydrodynamic properties and on light-scattering properties of DNA in solutions of various salt concentrations. Eisenberg derives a value of 28.5 nm for the nonelectrostatic bending persistence length of DNA. In fact, in an earlier modeling study, Schlick et al. [16] used a value of 31 nm for the elastic bending persistence length L_p, which is lower than the 50 nm value used in this study.

To estimate the effect of a lower value than that used in the results reported here, we have performed preliminary calculations with the value of $L_p = 28.5$ nm. We find that this lower value does not observably effect the predicted global structures at the extreme salt concentrations of 0.01 and 0.05 M reported in our work. For dinucleosomes at high salt, the mean core center-to-center distance is reduced from 16.33 with $L_p = 50$ nm to 16.28 with $L_p = 28.5$ nm, and the translational diffusion coefficients of small polynucleosomes are not affected in a statistically significant manner (i.e., values are the same within the error bars of the estimates). The geometric descriptors of the condensed fiber remain nearly identical in terms of radius of gyration and helical repeat.

In the absence of a universally accepted value for this parameter, further studies will need to carefully evaluate the sensitivity of modeling results to variations in L_p over the range of reported values.

Excluded volume parameters σ_1, σ_2, and k_{ex} are the only free parameters used in the model. We have shown [8] that the Debye-Hückel electrostatic potential is accurate at distances of greater than 1 nm at the salt concentration of $C_s = 0.05$ M. Thus, setting the core/core excluded volume distance parameter to $\sigma_2 = 2$ nm ensures that the potential remains fairly accurate and the charges are not allowed to overlap. The linker/core distance parameter is set to $\sigma_1 = 3$ nm to account for the approximate radius of double helical DNA.

Acknowledgments

Support by the National Science Foundation (ASC-9157582, ASC-9704681, BIR-9318159), the National Institutes of Health (R01 GM55164), and the John Simon Guggenheim Memorial Fund is gratefully acknowledged. We thank Qing Zhang for assisting in the electrostatic parameterization of the nucleosome core. T. S. is an investigator of the Howard Hughes Medical Institute.

Received: July 20, 2000
Revised: November 20, 2000
Accepted: November 23, 2000

References

1. van Holde, K. (1988). Chromatin (New York: Springer-Verlag).
2. Wolffe, A. (1995). Chromatin Structure and Function (San Diego: Academic Press).
3. van Holde, K., and Zlatanova, J. (1996). What determines the folding of the chromatin fiber? Proc. Natl. Acad. Sci. USA *93*, 10548–10555.
4. Woodcock, C.L., Grigoryev, S.A., Horowitz, R.A., and Whitaker, N. (1993). A chromatin folding model that incorporates linker variability generates fibers resembling the native structures. Proc. Natl. Acad. Sci. USA *90*, 9021–9025.
5. Finch, J.T., and Klug, A. (1976). Solenoidal model for superstructure in chromatin. Proc. Natl. Acad. Sci. USA *73*, 1897–1901.
6. Luger, K., Mader, A.W., Richmond, R.K., Sargent, D.F., and Richmond, T.J. (1997). Crystal structure of the nucleosome core particle at 2.8 Å resolution. Nature *389*, 251–260.
7. Schlick, T., Beard, D.A., Huang, J., Strahs, D., and Qian, X. (2000). Computational challenges in simulating large DNA over long times. IEEE Comp. Sci. Eng. *2*, 38–51.
8. Beard, D.A., and Schlick, T. (2001). Modeling salt-mediated electrostatics of macromolecules: the discrete surface charge optimization algorithm and its application to the nucleosome. Biopolymers *58*, 106–115.
9. Allison, S.A., Austin, R., and Hogan, M. (1989). Bending and twisting dynamics of short linear DNAs. Analysis of the triplet anisotropy decay of a 209 base pair fragment by Brownian simulation. J. Chem. Phys. *90*, 3843–3854.
10. Westcott, T.P., Tobias, I., and Olson, W.K. (1995). Elasticity theory and numerical analysis of DNA supercoiling: an application to DNA looping. J. Phys. Chem. *99*, 17926–17935.
11. Olson, W.K., Westcott, T.P., Martino, J.A., and Liu, G. (1996). Computational studies of spatially constrained DNA. In Mathematical Approaches to Biomolecular Structure and Dynamics, J.P. Mesirov, K. Schulten, and D.W. Sumners, eds. (New York: Springer-Verlag), pp. 195–121.
12. Martino, J.A., and Olson, W.K. (1997). Modeling protein-induced configurational changes in DNA minicircles. Biopolymers *41*, 419–430.
13. Ehrlich, L., Munkel, C., Chirico, G., and Langowski, J. (1997). A Brownian dynamics model for the chromatin fiber. CABIOS *13*, 271–279.
14. Shaw, S.Y., and Wang, J.C. (1993). Knotting of a DNA chain during ring closure. Science *260*, 533–536.
15. Rybenkov, V.V., Cozzarelli, N.R., and Vologodskii, A.V. (1993). Probability of DNA knotting and the effective diameter of the DNA double helix. Proc. Natl. Acad. Sci. USA *90*, 5307–5311.
16. Schlick, T., Li, B., and Olson, W.K. (1994). The influence of salt on the structure and energetics of supercoiled DNA. Biophys. J. *67*, 2146–2166.
17. Bednar, J., Furrer, P., Stasiak, A., Dubochet, J., Egelman, E.H., and Bates, A.D. (1994). The twist, writhe and overall shape of supercoiled DNA change during counterion-induced transition from loosely to tightly interwound superhelix. Possible implications for DNA structure in vivo. J. Mol. Biol. *235*, 825–847.
18. Lyubchenko, Y.L., and Shlyakhtenko, L.S. (1997). Visualization of supercoiled DNA with atomic force microscopy in situ. Proc. Natl. Acad. Sci. USA *94*, 496–501.
19. Yao, Y., Lowary, P., and Widom, J. (1990). Direct detection of linker DNA bending in defined-length oligomers of chromatin. Proc. Natl. Acad. Sci. USA *87*, 7603–7607.
20. Yao, Y., Lowary, P., and Widom, J. (1991). Linker DNA bending induced by the core histones of chromatin. Biochemistry *30*, 8408–8414.
21. Bednar, J., Horowitz, R.A., Dubochet, J., and Woodcock, C.L. (1995). Chromatin conformation and salt-induced compaction: three-dimensional structural information from cryoelectron microscopy. J. Cell Biol. *131*, 1365–1376.
22. Butler, P.J., and Thomas, J.O. (1980). Changes in chromatin folding in solution. J. Mol. Biol. *140*, 505–529.
23. McGhee, J.D., Nickol, J.M., Felsenfeld, G., and Rao, D.C. (1983). Higher order structure of chromatin: orientation of nucleosomes with the 30 nm chromatin solenoid is independent of species and spacer length. Cell *33*, 831–841.
24. Butler, P.J., and Thomas, J.O. (1984). A defined structure for the 30 nm fiber chromatin fiber which accommodates different nucleosomal repeat lengths. EMBO J. *3*, 2599–2604.
25. Fujiwara, S., Inoko, Y., and Ueki, T. (1989). Synchrotron x-ray scattering study of chromatin condensation induced by monovalent salt: analysis of the small-angle scattering data. J. Biochem. *106*, 119–125.
26. Fujiwara, S. (1992). Interpretation of the x-ray scattering profiles of chromatin at various NaCl concentrations by a simple chain model. Biophys. Chem. *43*, 81–87.
27. Greulich, K.O., Wachtel, E., Ausio, J., Seger, D., and Eisenberg, H. (1987). Transition of chromatin from the "10 nm" lower order structure, to the "30 nm" higher order structure as followed by small angle x-ray scattering. J. Mol. Biol. *193*, 709–721.
28. Jian, H. (1997). A combined wormlike-chain and bead model for dynamic simulations of long DNA. PhD thesis, New York University.
29. Bednar, J., et al., and Woodcock, C.L. (1998). Nucleosomes,

linker DNA, and linker histone form a unique structural motif that directs the higher-order folding and compaction of chromatin. Proc. Natl. Acad. Sci. USA *95*, 14173–14178.
30. Hagmann, M. (1999). How chromatin changes its shape. Science *285*, 1200–1203.
31. Staynov, D.Z. (1983). Possible nucleosome arrangements in the higher-order structure of chromatin. Int. J. Bio. Macromol *5*, 3–9.
32. Bordas, J., Perez-Grau, L., Koch, M.H.J., Vega, M.C., and Nave, C. (1986). The superstructure of chromatin and its condensation mechanism. II. Theoretical analysis of the X-ray scattering patterns and model calculations. Eur. J. Biophys. *13*, 175–185.
33. Williams, S.P., Athey, B.D., Muglia, L.J., Shappe, R.S., Gough, A.H., and Langmore, J.P. (1986). Chromatin fibers are left-handed double helices with diameter and mass per unit length that depend on linker length. Biophys. J. *49*, 233–248.
34. Garcia-Ramirez, M., Dong, F., and Ausio, J. (1992). Role of the histone 'tails' in the folding of oligonucleosomes depleted of histone H1. J. Biol. Chem. *267*, 19587–19595.
35. Braunstein, M., Rose, A.B., Holmes, S.G., Allis, C.D., and Broach, J.R. (1993). Transcriptional silencing in yeast is associated with reduced histone acetylation. Genes Dev. *7*, 592–604.
36. Hebbes, T.R., Thorne, A.W., and Crane-Robinson, C. (1988). A direct link between core histone acetylation and transcriptionally active chromatin. EMBO J. *7*, 1395–1402.
37. Hebbes, T.R., Thorne, A.W., Clayton, A.L., and Crane-Robinson, C. (1992). Histone acetylation and globin gene switching. Nucleic Acids Res. *20*, 1017–1022.
38. Hebbes, T.R., Clayton, A.L., Thorne, A.W., and Crane-Robinson, C. (1994). Core histone hyperacetylation co-maps with generalized DNase I sensitivity in the chicken β-globin chromosomal domain. EMBO J. *13*, 1823–1830.
39. Turner, B.M., Birley, A.J., and Lavender, J. (1992). Histone H4 isoforms acetylated at specific lysine residues define individual chromosomes and chromatin domains in Drosophila polytene nuclei. Cell *69*, 375–384.
40. Bone, J.R., Lavender, J., Richman, R., Palmer, M.J., Turner, B.M., and Kuroda, M.L. (1994). Acetylated histone H4 on the male X chromosome is associated with dosage compensation in Drosophila. Genes Dev. *8*, 96–104.
41. Sherratt, D. (1989). Tn3 and related transposable elements: site-specific recombination and transposition. In Mobile DNA, D.E. Berg and M.M. Howe, eds. (Washington, DC: American Society of Microbiology), pp. 163–184.
42. Goldstein, H. (1980). Classical Mechanics (Reading, MA: Addison-Wesley).
43. Schlick, T. (1995). Modeling superhelical DNA: recent analytical and dynamic approaches. Curr. Opin. Struct. Biol *5*, 245–262.
44. Jian, H., Vologodskii, A., and Schlick, T. (1997). A combined wormlike-chain and bead model for dynamic simulations of long linear DNA. J. Comp. Phys *136*, 168–179.
45. Stigter, D. (1977). Interactions of highly charged colloidal cylinders with applications to double-stranded DNA. Biopolymers *16*, 1435–1448.
46. Ermak, D.L., and McCammon, J.A. (1978). Brownian dynamics with hydrodynamic interactions. J. Chem. Phys. *69*, 1352–1360.
47. Heath, P.J., Clendenning, J.B., Fujimoto, B.S., and Schurr, J.M. (1996). Effect of bending strain on the torsion elastic constant of DNA. J. Mol. Biol. *260*, 718–730.
48. Baumann, C.G., Smith, S.B., Bloomfield, V.A., and Bustamante, C. (1997). Ionic effects on the elasticity of single DNA molecules. Proc. Natl. Acad. Sci. USA *94*, 6185–6190.
49. Eisenberg, H. (1998). Polyelectrolyte excluded volume and expansion compared to non-ionic polymers. ACTA Polymerica *49*, 534–538.
50. Cantor, C.R., and Schimmel, P.R. (1980). Biophysical Chemistry. Part III. The Behavior of Biological Macromolecules (New York: W. H. Freeman and Company).